

**Nuclear Magnetic Resonance Coherence Transfer
in a Homonuclear Two Spin-1/2 Solid-State System**

by

Deanne M. Taylor

A dissertation submitted in partial fulfillment
of the requirements for the degree of
Doctor of Philosophy
(Biophysics)
in The University of Michigan
2001

Doctoral Committee:

Assistant Professor A. Ramamoorthy, Chair
Professor Robert Sharp
Professor Erik R. P. Zuiderweg
Emeritus Distinguished Research Scientist W. Richard Dunham
Research Scientist Noemi Mirkin

When we try to pick out any thing by itself, we
find it hitched to everything else in the Universe.

JOHN MUIR

1838-1914

© Deanne M. Taylor 2001
All Rights Reserved

DEDICATION

No effort is completely autonomous. I dedicate this work to those who have helped me:

My parents, who lovingly and patiently waited for me
to get a 'real job' while supplying invaluable support and advice
My brother who brags about me behind my back.
My Nonie who loves and believes in me without question.
My Nana who sent me violets and secret money,
My Bapa for his indomitable spirit and wicked humor,
Auntie Redda whose wisdom and love is given freely,
My uncle **R** who had a lifetime love of learning and competition,
My uncle **T** who has had my diploma frame ready for years,
My son, for whom all things are possible.
The rest of "**The Family**", who stood behind me: **Auntie Mary, Auntie "Enis" & Uncle Alex,
Auntie C & Uncle T, Uncle K, Ally, Chris,** and everyone else.
My old friend and confidante, **Mark**, for laughter and email, and friends
Jay, Barry, Lark, Mary Pat, Al and Mia, all of whom kept me sane.

My advisor, **Dr. A. Ramamoorthy**, for giving me the chance to succeed,
My thesis committee: **Drs. W.R. Dunham, Noemi Mirkin, Robert Sharp and E.R.P. Zuiderweg**,
for advice, genuine caring, support, good humor and the occasional FORTRAN program,
Lecturer Nancy Kerner for her unequalled encouragement and visionary example,
Drs. Frank Day, Tom Bourke, Marie Clarke, Wendy Hagen Bauer, Richard French, Yue Hu, Judith Brown.

Ms. Ruby, who stood by me from day minus one,
Dr. Richard Goldstein, for his good heart and wise advice,
Drs. Robert Zand and **Cynthia Marcelo** for the afternoon chats,
Dr. Dan Axelrod for the qualities that make him a good person and scientist,
and the Biophysics Faculty and Associated Faculty at the University of Michigan.

My labmates - **Jeff "CIA" Brender, Jose "Jazz And Truth" Santos, Kevin "It's a Conspiracy"
Hallock, Katie "Polly Alanine" Henzler, Dr. Duane "Eat my Spectra" Chung, Dr. "Shake and Bake"
Shekar, Dr. Dongkuk Lee, Dr. Yu-Feng Wei, Mr. Michael Dehring, Mr. Srikanth Kidambi.**

My fellow scientists - **Drs. Namdo Moon, Thomas Butler, Darrin "The Finch Master" Taverna,
Maricel Kann, Craig Smith, Peter Cabauy, Liz Rhodes, Nick Buschler, Nat Schaeffle, and Yuxi
Peng, none of whom were buried with a bottle of tequila.**

*And last, but not least, for Ms. Dorothy Jaeger of UMBS, who gives chocolate and kind words to late-night
graduate students.*

ACKNOWLEDGEMENTS

I wish to acknowledge the invaluable help and financial support of the University of Michigan's Center for the Education of Women for the 1998 and 1999 Sloan Summer Fellowship, and the 1997 Margaret Dow Towsley Scholarship, as well as various help from several funds within the Center. This assistance eased the non-academic challenges and allowed me to concentrate on the work at hand to finish this dissertation in a timely manner. I owe a debt reaching well past the fiduciary, in the priceless humanity, generosity, humor, support, wisdom, and kind words from the CEW colleagues to another of the many female graduate students at this University. Thank you.

We also would like to acknowledge the support from the NSF Career Development Award for Dr. Ramamoorthy, as well as the Petroleum Research Fund from the American Chemical Society, all of whose support helped fund this research.

TABLE OF CONTENTS

DEDICATION.....	ii
ACKNOWLEDGEMENTS.....	iii
LIST OF TABLES	vi
LIST OF FIGURES.....	vii
LIST OF APPENDICES	xiv
LIST OF ABBREVIATIONS USED	xv
1. INTRODUCTION.....	1
2. CHARACTERISTICS OF COHERENCE TRANSFER THROUGH INTERNAL HAMILTONIANS	9
Introduction to Spin Operators.....	11
Characteristics of the Spin Component of the Dipolar Hamiltonian.....	16
Rotation and Commutation of Operators and the Dipolar Hamiltonian.....	17
Characteristics of the Spatial Component of the Dipolar Hamiltonian.....	21
3. DIPOLAR-COUPLING-MEDIATED COHERENCE TRANSFER IN A HOMONUCLEAR TWO SPIN ½ SOLID STATE SYSTEM.....	23
Abstract	23
Introduction.....	24
Theory.....	25
Results and Discussion.....	32
Conclusions	46
Acknowledgements.....	47
4. DIPOLAR-COUPLING-MEDIATED COHERENCE TRANSFER IN AN UNORIENTED HOMONUCLEAR TWO SPIN-½ SOLID STATE SYSTEM.....	48
Abstract	48
Introduction.....	49
Theory of the Static Dipolar Hamiltonian.....	50
Methods.....	52
Results and Discussion.....	54
Unoriented Sample Simulation for H_D	54
The DRAMA Experiment	73
The DRAWS Experiment.....	84
The RFDR Experiment.....	91

The USEME Experiment	99
Conclusions	105
5. DIPOLAR COHERENCE TRANSFER IN THE PRESENCE OF CHEMICAL SHIFT FOR UNORIENTED AND ORIENTED HOMONUCLEAR TWO SPIN-$\frac{1}{2}$ SOLID STATE SYSTEMS	110
Introduction.....	110
Theory for an Oriented Strongly Coupled System.....	113
The Full Free-Precession Hamiltonian for a strongly coupled oriented sample	116
Transformation of the Spin Part of H_F	121
Methods.....	124
Results and Discussion.....	124
Effects of chemical shift coherence transfer in unoriented samples: calculations from the tilted frame.....	125
Conclusions	154
6. CONCLUSIONS AND FUTURE DIRECTIONS	156
APPENDICES	158
BIBLIOGRAPHY	199

LIST OF TABLES

Table 2-1: The two-spin operators as density matrices.....	14
Table 2-2: The definition of the subgroups generated by a Hamiltonian in a two-spin-1/2 space . We have not included the negative forms of the operators for brevity but it should be assumed that all members of the subgroups include all negative forms of the operators.	19
Table 2-3: Inner product (dot product) group characteristic table for I_x group matrices. 20	20
Table 2-4: Inner product (dot product) group characteristic table for I_y group matrices. 20	20
Table 2-5: Inner Product (dot product) group characteristic table for I_z group matrices. 20	20
Table 3-1: Expectation values of operators evolving under the dipolar and scalar coupling Hamiltonians. The initial states are given in the leftmost column. The evolving states are to be read across the row. For instance, I_x evolves to $A I_x + B S_x - E I_y S_z + F I_z S_y$. The values of A-G are given in Table 2.	34
Table 4-1 (this and next page): (a) Expectation values of operators evolving under the dipolar and scalar Hamiltonian. The initial states are given in the leftmost column. The evolving states are to be read across the row. For instance, I_x evolves to $A I_x + B S_x - E I_y S_z + F I_z S_y$	55
Table 4-1(b). Values of coefficients A-G in Table 4-1a.....	56
Table 4-2 (this and next page): (a) Expectation values of operators evolving under the DRAMA coupling Hamiltonians. The initial states are given down the leftmost column. The evolving states are to be read across the row. For instance, I_x evolves to $A I_x - B S_x - E(I_y S_z + I_z S_y)$	75
Table 4-2(b): Coefficients of the spin operators generated due to the evolution under H_{DRAMA}	76
Table 4-3: (this and next page): (a) Expectation values of operators evolving under the DRAWS coupling Hamiltonian. The initial states are given down the leftmost column. The evolving states are to be read across the row. For instance, I_x evolves to $A I_x + B S_x - C I_y S_z + D I_z S_y$	86
Table 4-3(b) Coefficients of the spin operators generated due to the evolution under H_{DRAWS} . $\alpha = 2c_{zz}$, $\beta = c_{xx} - c_{zz}$, $\gamma = -(c_{xx} + c_{zz})$	87
Table 4-4: (this and next page): (a) Expectation values of operators evolving under the RFDR coupling Hamiltonian. The initial states are given down the leftmost column. The evolving states are to be read across the row. For instance, I_x evolves to $A I_x + B I_z S_y$	94
Table 4-4(b): Coefficients of the spin operators generated due to the evolution under H_{RFDR} (Table 4-4(a)).....	95
Table 4-5: (this and next page): (a) Expectation values of operators evolving under the USEME coupling Hamiltonian. The initial states are given down the leftmost column. The evolving states are to be read across the row. For instance, I_x evolves to $A I_x + B S_x - E I_y S_z + F I_z S_y$	101
Table 4-5(b): Coefficients of the spin operators generated due to the evolution under H_{USEME}	102
Table 4-6: Summary of position and velocity coefficients for maximum-peak DCT for several recoupling experiments as compared to the static unoriented powder sample	108

LIST OF FIGURES

- Figure 2-1:** Operators important to NMR transitions. Compare with the individual operators shown in Table 2-1. (a) Density matrix from the Pauli spin matrices with the notation for I and S operators included. The usual convention, that of α "spin down" and β "spin up" applies. (b) the meanings of each of the operators in terms of population (Pop), single quantum I or S (SQ I, SQ S), zero quantum (ZQ) and double quantum (DQ) populations. Space-saving notation $X_{nm}Y_{nm}$ means to include all combinations of operators in that element, as an example $I_{x,y}S_{x,y}$ which stands for operators I_xS_y , I_yS_x , I_xS_x , I_yS_y 13
- Figure 3-1** (a-g, this and subsequent pages): Expectation values of various spin operators under the dipolar coupling Hamiltonian, H_D (solid lines), and the total coupling Hamiltonian, H_{JD} (dotted and dashed lines). The coefficients of the spin operators given in Table 2-1 are plotted as a function of evolution time in an oriented or single crystal system containing two ^{13}C nuclei separated by a distance of 1.55 Å. The dotted lines are for $J = -53$ Hz and the dashed lines are for $J = 53$ Hz. For example, in (a), the magnitude of the term A is plotted as a function of the evolution time under the Hamiltonian H_{JD} . This can be used to evaluate the amount of magnetization which remains in the source or in I nuclei when x magnetization of the I nuclei is selected for the coherence transfer under the coupling Hamiltonian. Similarly, in (b), the magnitude of the term B is plotted as a function of the evolution time under the Hamiltonian H_{JD} . This can be used to evaluate the amount of magnetization transferred to the S nuclei when x magnetization of the I nuclei is selected for the coherence transfer under the coupling Hamiltonian. 28
- Figure 3-2** (this and following page) (a) Three-dimensional plot showing the dependence of the expectation value of the I_x operator during the evolution of the I_x operator under the H_D Hamiltonian (as given by the term A in Table 1) on the dipolar coupling and the evolution time. Two-dimensional slices (b), (c), and (d) taken from the three-dimensional plot in (a) for the evolution times 2, 5, and 10 ms, respectively, are shown for $J = 0$ (solid lines) and for $J = 53$ Hz (dashed lines). 35
- Figure 3-3** (this and following page). (a) Three-dimensional plot showing the dependence of the expectation value of the S_x operator during the evolution of the I_x operator under the H_D Hamiltonian (as given by the term B in Table 1) on the dipolar coupling and the evolution time. Two-dimensional slices (b), (c), and (d) taken from the three-dimensional plot in (a) for the evolution times 2, 5, and 10 ms, respectively, are shown for $J = 0$ (solid lines) and for $J = 53$ Hz (dashed lines).system under the H_{JD} Hamiltonian. Two-dimensional slices in Figs. 3-2b to 3-2d are taken from the three-dimensional plot in Fig. 3-2a for various evolution times, while varying the dipolar coupling from 0 to 23 kHz. The dependence of the terms B, C, and D on the dipolar coupling and the evolution time are presented in Figs. 3-3, 3-4, and 3-5, respectively. 39
- Figure 3-4** (this and following page) (a) Three-dimensional plot showing the dependence of the expectation value of the I_z operator during the evolution of the I_z operator under the H_{JD} Hamiltonian (as given by the term C in Table 1) on the dipolar coupling and the evolution time. Two-dimensional slices (b), (c), and (d) taken from

the three-dimensional plot in (a) for the evolution times 2, 5, and 10 ms, respectively, are shown for $J = 0$ (solid lines) and for $J = 53$ Hz (dashed lines).	41
Figure 3-5 (this and following page) (a) Three-dimensional plot showing the dependence of the expectation value of the S_z operator during the evolution of the I_z operator under the H_D Hamiltonian (as given by the term D in Table 1) on the dipolar coupling and the evolution time. Two-dimensional slices (b), (c), and (d) taken from the three-dimensional plot in (a) for the evolution times 2, 5, and 10 ms, respectively, are shown for $J = 0$ (solid lines) and for $J = 53$ Hz (dashed lines).....	43
Figure 3-6 Three-dimensional plots showing the dependence of the terms A, B, C, and D on the ratio of the scalar and dipolar couplings are shown in (a), (b), (c), and (d), respectively. The dipolar coupling was assumed to be 100 Hz.	45
Figure 4-1 (a-g) (this and subsequent pages): Simulations of the expectation values of the operators modulated by functions A-G (Table 4-1) of an unoriented system allowed to evolve freely under H_D . The y-axis is normalized magnetization (1=100%). Simulations assumed two ^{13}C nuclei at a typical glycine $\text{C}_\text{O}-\text{C}_\alpha$ distance of $r_{\text{CS}} = 1.53\text{\AA}$ corresponding to a dipolar coupling $D_{\text{CC}} = 2120.7$ Hz.....	56
Figure 4-2: The FFT of the simulation of the time domain coherence transfer function C (Figure 4-1(c)). No window function has been used in FFT. This is the Pake doublet powder pattern spectrum due to the longitudinal DCT.	60
Figure 4-3 (a-b). The spherical plot representation of the spatial part of the homonuclear dipolar coupling Hamiltonian. (a) The principle-axis system representation (Eq. 4-2). (b) The spatial part of the dipolar Hamiltonian after the transformation to the laboratory frame.	60
Figure 4-4 (a-d) (this and next page). (a) Three-dimensional plot showing the dependence of the expectation value of Function A in Table 4-1, representing the transverse self-magnetization retained by the first spin through DCT in an unoriented two-spin ^{13}C homonuclear system, for example when $\sigma(0) = I_x$. Two-dimensional slices (b), (c), and (d) are taken from the three-dimensional plot in (a) for the evolution times 2, 5, and 10ms respectively, shown for $J=0$ (solid lines) and $J=53$ Hz (dashed lines). normalized magnetization.....	64
Figure 4-5 (a-d) (this and following page). (a) Three-dimensional plot showing the dependence of the expectation value of Function B in Table 4-1, representing the transverse magnetization transferred to the second spin through DCT in an unoriented two-spin ^{13}C homonuclear system, for example when $\sigma(0) = I_x$. Two-dimensional slices (b), (c), and (d) are taken from the three-dimensional plot in (a) for the evolution times 2, 5, and 10ms respectively, shown for $J=0$ (solid lines) and $J=53$ Hz (dashed lines). normalized magnetization.....	66
Figure 4-6 (a-d) (this and following page). (a) Three-dimensional plot showing the dependence of the expectation value of Function C in Table 4-1, representing the longitudinal self-magnetization retained by the first spin through DCT in an unoriented two-spin ^{13}C homonuclear system, for example when $\sigma(0) = I_z$. Two-dimensional slices (b), (c), and (d) are taken from the three-dimensional plot in (a) for the evolution times 2, 5, and 10ms respectively, shown for $J=0$ (solid lines) and $J=53$ Hz (dashed lines). normalized magnetization.....	68
Figure 4-7 (a-d) (this and following page). (a) Three-dimensional plot showing the dependence of the expectation value of Function D in Table 4-1, representing the	

longitudinal magnetization transferred to the second spin through DCT in an unoriented two-spin ^{13}C homonuclear system, for example when $\sigma(0) = I_z$ Two-dimensional slices (b), (c), and (d) are taken from the three-dimensional plot in (a) for the evolution times 2, 5, and 10ms respectively, shown for $J=0$ (solid lines) and $J=53$ Hz (dashed lines). normalized magnetization..... 70

Figure 4-8 (a-b): (a) The trace of maximum coherence diffusion peak of Function D in Table 4-1, representing the maximum transferred longitudinal magnetization to the second spin in an unoriented two-spin ^{13}C homonuclear system, for example when $\sigma(0) = I_z$. $r = 2.67 t^{1/3}$ Scalar coupling was assumed to be zero. (b) The rate of coherence transfer, ν , versus mixing time ($\text{\AA}/\text{ms}$). $\nu = 0.89 t^{-2/3}$ 72

Figure 4-9: The DRAMA pulse sequence..... 74

Figure 4-10: Powder-averaged expectation values for operators evolving with coefficients A, B, and C from Table 4-2 for $\tau/\tau_r = 0.50$ for a ^{13}C homonuclear system as a function of DRAMA experimental time, $r_{IS}=1.53\text{\AA}$ 78

Figure 4-11: Dependence of DCT magnitude on the ratio of τ/τ_r for a series of experimental times for the powder-averaged expectation value $\langle S_x \rangle$ corresponding to the DCT coefficient B in Table 4-2. Continuation of this graph to $\tau/\tau_r = 1$ causes the curves to mirror around $\tau/\tau_r = 0.5$ 78

Figure 4-12: Transformation of the spatial part of the DRAMA Hamiltonian when varying τ/τ_r for values of τ/τ_r for (a) 0.1 (b) 0.2 (c) 0.3 (d) 0.4 (e) 0.5. 81

Figure 4-13: An implicit graph of the maximum coherence transfer (first maximum $>50\%$) in a DRAMA pulse sequence, for internuclear distance and the ratio of τ/τ_r as a function of experimental time. The implicit maximum trends between 52% and 63% of normalized magnetization, which is correlated to the value of τ/τ_r 82

Figure 4-14: (a) The trace of maximum coherence diffusion peak ($r = 1.41 t^{1/3}$) of Function B in Table 4-2, representing the maximum transferred transverse magnetization to the second spin in a DRAMA experiment as a function of experimental time where $\tau/\tau_r=0.5$, for example when $\sigma(0) = I_x$. (b) The rate of coherence transfer, ν_{DRAMA} , versus experimental time ($\text{\AA}/\text{ms}$). $\nu_{\text{DRAMA}} = 0.47 t^{-2/3}$ 83

Figure 4-15: The spatial component of the DRAWS Hamiltonian. (all normalized) (a) the c_{xx-yy} term, showing the mix of yz and x^2-y^2 forms in the coefficient. (b) the c_{zz} term, which is dominated by the yz term rather than the x^2-y^2 term. (c) the x^2-y^2 term and (d) the yz terms directly from the c-coefficients of DRAWS. 85

Figure 4-16: The DRAWS pulse sequence, with continuous rf irradiation applied between two $\pi/2_y$ pulses..... 87

Figure 4-17: DRAWS coherence transfer coefficients from Table 4-3 for a ^{13}C homonuclear system as a function of DRAWS experimental time. $r_{IS}=1.53\text{\AA}$. (a) A, B, C and D. (b) E, F..... 88

Figure 4-18: The powder-averaged expectation value $\langle I_y + S_y \rangle$ (solid line) corresponding to the sum of DCT coefficients E+F, and $\langle I_x + S_x \rangle$ (dotted line) corresponding to the sum of DCT coefficients A+B, plotted as a function of DRAWS irradiation time. Note the internuclear distance for both traces is $r_{IS} = 2.39 \text{\AA}$, for purposes of comparison to reference [57]..... 89

Figure 4-19: (a) The trace of the maximum coherence diffusion peak ($r = 1.51 t^{1/3}$) of Function F in Table 4-2, as a function of DRAWS irradiation (mixing) time, representing the maximum transferred transverse magnetization to the second spin in

- a DRAWS experiment, for example when $\sigma(0) = I_y$. (b) The rate of coherence transfer, ν_{DRAWS} as a function of experimental time ($\text{\AA}/\text{ms}$). $\nu_{\text{DRAWS}} = 0.503 t^{-2/3}$. 90
- Figure 4-20:** The RFDR pulse sequence. The phase of the π pulses are alternated in experiment over the period n 93
- Figure 4-21:** Effective coupling dRFDR vs. the dimensionless parameter of $\nu_r / \Delta\delta$ for two model crystallite orientations (Eq.4-10). For the $m=1$ curve, $d_{2,|1|}(\beta) = 2153 \text{ Hz}$ and $d_{2,|2|}(\beta) = 0 \text{ Hz}$, and for the $m=2$ curve, $d_{2,|1|}(\beta) = 0 \text{ Hz}$ and $d_{2,|2|}(\beta) = 2153 \text{ Hz}$. $\gamma = 0$ in both cases..... 93
- Figure 4-22:** RFDR coherence transfer coefficients A, B, C and D. from Table 4-4 for a ^{13}C homonuclear system where $r_{\text{IS}} = 1.53 \text{\AA}$. Plots are a function of RFDR experimental time. (a) With $\Delta\delta/\nu_r = 1.0$, Note the coefficient B remains close to zero. (The coefficient E is approximately zero for all time in the powder average so does not appear here) (b) With $\Delta\delta/\nu_r = 1.5325$, approximately where the two lines in Figure 4-21 have equal values..... 96
- Figure 4-23:** Parametric plots of the frequency distribution of dRFDR, normalized relative to the maximum dipolar coupling constant for the experiment. (a) $\Delta\delta/\nu_r = 1.0$ (b) $\Delta\delta/\nu_r = 0.5$ (c) $\Delta\delta/\nu_r = 1.5625$ (as in Figure 4-22(b)). (d) $\Delta\delta = \Omega_I - \Omega_S = 123 \text{ ppm}$, $\nu_r = 3.33 \text{ kHz}$ ($\Delta\delta/\nu_r = 3.92$) ($\Delta\delta/\nu_r = 1.86$) (e) $\Delta\delta/\nu_r = 2.61$, corresponding to $\nu_r = 5.0 \text{ kHz}$ and $\Delta\delta = \Omega_I - \Omega_S = 123 \text{ ppm}$. (f) The same system as (e) but with a integral spread ranging over $1.2 (\Omega_I - \Omega_S)$, corresponding to a field inhomogeneity of 24.6 ppm 97
- Figure 4-24:** (a) The trace of maximum coherence diffusion peak ($r = 1.84 t^{1/3}$) of Function D in Table 4-4, representing the maximum transferred transverse magnetization to the second spin in a RFDR experiment as a function of experimental time, for example when $\sigma(0) = I_z$. (b) The rate of coherence transfer, ν_{RFDR} , versus experimental time ($\text{\AA}/\text{ms}$). $\nu_{\text{RFDR}} = 0.61 t^{-2/3}$ 98
- Figure 4-25:** The USEME pulse sequence. The spin-echo (SE) sequence refocuses the chemical shift, while the magic echo (ME) recouples the dipolar interaction. 102
- Figure 4-26:** Parametric plot of the frequency distribution of d_{USEME} , normalized relative to the maximum dipolar coupling constant for the experiment. 103
- Figure 4-27:** USEME coherence transfer coefficients from Table 4-4 for a ^{13}C homonuclear system as a function of USEME experimental time. $r_{\text{IS}} = 1.53 \text{\AA}$ for the coefficients A, B, C, D. The coefficients E, F, and G are approximately zero for all time in the powder average so do not appear in this graph..... 103
- Figure 4-28:** (a) The trace of maximum coherence diffusion peak ($r = 1.51 t^{1/3}$) of Function D in Table 4-5, representing the maximum transferred transverse magnetization to the second spin in a USEME experiment as a function of experimental time, for example when $\sigma(0) = I_z$. (b) The rate of coherence transfer, ν_{USEME} , versus experimental time ($\text{\AA}/\text{ms}$). $\nu_{\text{USEME}} = 0.50 t^{-2/3}$ 104
- Figure 4-29:** Coherence transfer compared for all MASDR experiments over 10 ms. Solid line: unoriented sample. Long-dashed line: RFDR. Short dashed line: USEME and DRAWS. Dense dotted line: DRAMA. (a) The trace of maximum coherence diffusion for several dipolar-recoupling experiments. (b) The instantaneous velocity of dipolar coherence transfer, ν , for the same range of mixing times. 106

- Figure 4-30:** Distance of maximum DCT peak as a function of experimental mixing time over a range of distances relevant to peptide backbone $^{13}\text{C}_\alpha - ^{13}\text{C}_\text{O}$ experiments. Data key is labeled above each series. For DRAMA, $\Delta\delta/\nu_I=0.5$; for RFDR, $m=1$. USEME and DRAWS are essentially identical. 107
- Figure 5-1:** Example results for the chemical shift frequency A_0^{LAB} for spin I in the laboratory frame after transformation from the principal axis system. The angles relating the CS PAS to the molecular frame were assigned the values $\alpha_I=5^\circ$, $\beta_I=20^\circ$, $\gamma_I=25^\circ$ with the values of the chemical shift for spin I being $\sigma_{11}^I=46.8\text{ppm}$, $\sigma_{22}^I=3.8\text{ppm}$, and $\sigma_{33}^I=73.2\text{ppm}$, with $\sigma_I=1/3(\sigma_{11}^I + \sigma_{22}^I + \sigma_{33}^I)$ 112
- Figure 5-2.** The coordinate system for the rotation to the "tilted frame" that uses the operator $(I_x S_y - I_y S_x)$, which commutes with both $\Delta(I_z - S_z)$ and $B(I_x S_x + I_y S_y)$. The transformation is achieved by a rotation angle θ around $(I_x S_y - I_y S_x)$. See Eq. 5-20 and following for definitions of the constants..... 123
- Figure 5-3.** A graph of the value of $\frac{\Delta}{R}$ where $R=\sqrt{\Delta^2 + B^2}$, as a function of dipolar coupling and Δ , where $(B=2\pi J-D)$.. (a) $J=0\text{ Hz}$. Note the fast shoulder at $D=\Delta=0$. (b) $J=53\text{Hz}$. Since J is of opposite sign to D , term $\frac{\Delta}{R}$ reaches the value of "1" for larger values of Δ 127
- Figure 5-4:** Graph of the "odd term" in I_x for an oriented sample, Eq. , as a function of the chemical shift average frequency in the lab frame (Σ) and chemical shift difference in the lab frame (Δ) where $t=1\text{ms}$, and the internuclear distance $r=1.53\text{\AA}$. The scalar coupling $J=0$ 128
- Figure 5-5:** Graph of the "odd term" in I_x for an oriented sample, as a function of the dipolar coupling frequency in the lab frame in kHz, and the chemical shift difference in the lab frame (Δ) where $t=3\text{ms}$, and the CS average frequency in the lab frame is $\Sigma=50\text{ ppm}$. The scalar coupling $J=0$ 129
- Figure 5-6:** Graph of the "odd term" in I_x for an oriented sample, as a function of the dipolar coupling frequency in the lab frame in kHz, and the chemical shift average in the lab frame (Σ) where $t=3\text{ms}$, and the CS difference frequency in the lab frame is $\Delta=50\text{ ppm}$. The scalar coupling $J=0$ 130
- Figure 5-7:** Graph of the "even term" for I_x for an oriented sample, as a function of the dipolar coupling frequency in the lab frame in kHz, and the chemical shift average in the lab frame (Σ) where $t=3\text{ms}$. The scalar coupling $J=0$ 131
- Figure 5-8:** Graph of the CT function for S_x when $\sigma(0)=I_x$ for an oriented sample,, as a function of the dipolar coupling frequency in the lab frame in kHz, and the chemical shift average in the lab frame (Σ) where $t=1\text{ms}$, and the CS difference frequency in the lab frame is $\Delta=0\text{ ppm}$. The scalar coupling $J=0$. See Eq. 5-21. 132
- Figure 5-9:** Graph of the CT function for S_x when $\sigma(0)=I_x$ for an oriented sample,, as a function of the dipolar coupling frequency in the lab frame in kHz, and the chemical shift average in the lab frame (Σ) where $t=5\text{ms}$, and the CS difference frequency in the lab frame is $\Delta=0\text{ ppm}$. The scalar coupling $J=0$. See Eq. 5-21. 133
- Figure 5-10:** Graph of the CT function for S_x when $\sigma(0)=I_x$ for an oriented sample,, as a function of the dipolar coupling frequency in the lab frame in kHz, and the chemical

shift average in the lab frame (Σ) where $t=5\text{ms}$, and the CS difference frequency in the lab frame is $\Delta=50$ ppm. The scalar coupling $J=0$. See Eq. 5-21.	134
Figure 5-11: Graph of the CT function for the I_x self-magnetization, when $\sigma(0)=I_x$ for an oriented sample, as a function of the dipolar coupling frequency in the lab frame in kHz, and the chemical shift difference Δ in the lab frame where $t=3\text{ms}$, and the CS average frequency in the lab frame is set as $\Sigma =50$ ppm. The scalar coupling $J=0$.	135
Figure 5-12: Graph of the CT function for the I_x self-magnetization for an oriented sample, when $\sigma(0)=I_x$, as a function of the dipolar coupling frequency in the lab frame in kHz, and the chemical shift average Σ in the lab frame where $t=3\text{ms}$, and the CS average frequency in the lab frame is set as $\Delta=50\text{ppm}$; The scalar coupling $J=0$.	136
Figure 5-13: Graph of the CT function for the I_x self-magnetization for an oriented sample, when $\sigma(0)=I_x$, as a function of the dipolar coupling frequency in the lab frame in kHz, and the chemical shift difference is set to $\Delta=120\text{ppm}$ and the CS average frequency (both in the lab frame) is set as $\Sigma =80$ ppm. The scalar coupling $J=0$. Time is in ms.	137
Figure 5-14: Graph of the CT function for the I_z self-magnetization for an oriented sample, when $\sigma(0)=I_z$, as a function of time and the chemical shift difference Δ in ppm. The dipolar coupling is set to correspond to an internuclear distance of 1.53 \AA . The scalar coupling $J=0$. Time is in ms.	142
Figure 5-15: Graph of the CT function for the S_z transferred-magnetization for an oriented sample, when $\sigma(0)=I_z$, as a function of time and the chemical shift difference Δ in ppm. The dipolar coupling is set to correspond to an internuclear distance of 1.53 \AA . The scalar coupling $J=0$. Time is in ms.	143
Figure 5-16: Graph of the CT function for the I_z self-magnetization for an oriented sample, when $\sigma(0)=I_z$, as a function of dipolar coupling frequency in kHz and the chemical shift difference Δ in ppm. The constant time is set to 5ms. The scalar coupling $J=0$	144
Figure 5-17: Graph of the CT function for the S_z transferred coherence for an oriented sample, when $\sigma(0)=I_z$, as a function of dipolar coupling frequency in kHz and the chemical shift difference Δ in ppm. The constant time is set to 5ms. The scalar coupling $J=0$	145
Figure 5-18: Graph of the CT function for the I_x self-magnetization of an unoriented sample, when $\sigma(0)=I_x$, as a function of time. The parameters are given below. All three simulations share the listed constants, with specific principal values given below: The Euler angles were chosen arbitrarily. Note that the “chaotic” behavior of the dephasing is not due to the limits of resolution.	149
Figure 5-19: Graph of the CT function for the S_x (transferred) self-magnetization for an unoriented sample, when $\sigma(0)=I_x$, as a function of time. The parameters are given below. Note that the “chaotic” behavior of the dephasing is not due to the limits of resolution. Euler angles were chosen arbitrarily. Note that the “chaotic” behavior of the dephasing is not due to the limits of resolution.	150
Figure 5-20: Graph of the CT function for the I_x self-magnetization for an unoriented sample, when $\sigma(0)=I_x$, as a function of time for two sets of principle values of the	

chemical shift. The parameters are given below. Note that the “chaotic” behavior of the dephasing is not due to the limits of resolution..... 151

Figure 5-21: Graph of the CT function for the I_x self-magnetization for an unoriented sample, when $\sigma(0)=I_x$, as a function of time for three sets of principal values of the chemical shift. The parameters are given below. Note that the “chaotic” behavior of the dephasing is not due to the limits of resolution..... 152

Figure 5-22: Graph of the CT function for the I_x self-magnetization for an unoriented sample, when $\sigma(0)=I_x$, as a function of time for three sets of principal values of the chemical shift. The parameters are given below..... 153

LIST OF APPENDICES

Appendix

- A. Some programs used in generating this thesis.158

LIST OF ABBREVIATIONS USED

CT	Coherence Transfer
DCT	Dipolar Coherence Transfer
DRAMA.....	Dipolar Recoupling At the Magic Angle
DRAWS	Dipolar Recoupling with A Windowless Sequence
LAB	Laboratory Frame of Reference
MAS	Magic-Angle sample Spinning (or just Magic Angle Spinning)
MASDR.....	Magic-Angle Spinning Dipolar Recovery
NMR.....	Nuclear Magnetic Resonance
RF	Radio Frequency
RFDR	Radio Frequency-driven Dipolar Recoupling
RINEPT.....	Refocused *** Enhanced Polarization Transfer
SEDRA.....	Simple Excitation for the Dephasing of Rotational-echo Amplitudes
SSNMR.....	Solid State Nuclear Magnetic Resonance
USEME.....	Unified Spin Echo Magic Echo

CHAPTER 1 INTRODUCTION

There are numerous biological problems of interest that cannot be easily studied by the more conventional methods of crystallography or solution-state nuclear magnetic resonance (NMR). Examples would be the conformational changes of a membrane-bound receptors on substrate binding, the conductive and selective mechanisms of ion and protein channels [1-6], key structural information for large water-soluble proteins with small rotational diffusion constants [7], orientation and structural information of hydrophobic proteins embedded in micelles [8-11], protein-lipid interactions necessary for proper protein function [6, 12-15], and fibrous peptides such as amyloidogenic peptide proteins [16], silk [17], and collagen [18]. The list is actually much larger, and as a representative selection, has left out many important contributions to the field of nuclear magnetic resonance (NMR) structural biology in the interest of space.

There are many such insoluble systems that pose interesting problems, yielding some information only after long and expensive molecular biology experiments. Membrane proteins are heavily processed before they enter their functional environment and do not lend themselves to straightforward study using conventional spectroscopic methods. Because of their insolubility, more indirect measures of their structural and functional properties are left to expensive procedures, such as mutagenesis studies. Solid-state NMR (SSNMR) methods are well-suited to study such difficult systems, and the technique is becoming increasingly important for the study of complex biological molecules. A current (and excellent) review on protein and polypeptide structure and SSNMR is by Fu and Cross [19].

To enhance sensitivity, many experiments in SSNMR are done on molecules labeled with spin-1/2 isotopes such as ^{13}C or ^{15}N at specific sites [2, 10, 13, 20-24]. The need for specific labeling and the strong interactions that affect SSNMR experiments may be some of the reasons that the experimental method has lagged behind the development of solution-state NMR.. A historical account of SSNMR can be found in Andrew and Szczesniak [25], but it would not be an exaggeration to say that much of the methodology in SSNMR has not changed in over a decade.

It would be of great advantage to the research community if one or more straightforward SSNMR methods are developed to solve biological macromolecular structures using special isotopes at non-specific, uniformly labeled sites or residues [26], as it would allow structural studies of many proteins inaccessible by any other methods, with the advantage that these proteins would be produced and naturally post-translationally processed *in vivo* [27]. Unfortunately, the cost of preparing an NMR experimental sample from a cell culture for an isotopically-labeled protein at specific residues is likely as or more expensive than established mutagenesis procedures.

Structural information on membrane proteins would not only benefit academic research but also health and medicine; membrane proteins are often the targets of drug therapies, and take on a diverse number of receptor roles for substrates, such as cytokines, growth factors, chemokines, stress and apoptosis signals [28], bioactive peptides, matrix peptides, and cell-to-cell signaling proteins, not to mention additional roles as ion channels and antimicrobial pore-forming peptides.

It is understood by those in the pharmaceutical industry that one of the largest roadblocks to development and research into therapeutic targets is the lack of active site information for the largest target family: seven-helix transmembrane receptors (7TMRs), which are insoluble membrane proteins involved in initiation of internal cellular signals [29]. Attempts to characterize unknown 7TMRs by sequence alignment with ligand-characterized 7TMRs are seldom successful at predicting the unknown's function or

ligand binding affinities, unless obvious, close sequence homologies exist between the target sequence and the established sub-families. This is rarely the case. For instance, because of the difficulty in linking sequence information to actual function and ligand class, there are hundreds of putative "orphan" G-protein coupled receptors (GPCRs) which have no known endogenous ligand, and whose presence is postulated due to strong hydrophobicity signatures that may indicate seven transmembrane helices in translated genomic sequences [30]. Undiscovered and orphan GPCRs are the targets of an all-out discovery match between large and small pharmaceutical companies alike.

Because there is mutagenesis evidence for several "deep" (i.e. partially transmembrane-helix-lined) binding pockets for some of the known GPCRs [31], the question of ligand binding cannot be simply addressed by extracellular domain modeling; the entire structure of the protein must be known as the helices do not always act in a simple structural-scaffolding type role [32]. Some advantage in homology modeling has been gained with the recent and valuable structure of the GPCR rhodopsin at 2.8 Angstroms [33]. This structure has been exploited by structural biologists for homology modeling of other 7TMRs [34] with limited predictive results, likely due to the fact that rhodopsin does not have a surface-accessible ligand binding site, but rather a deep chromophore binding pocket between the transmembrane helices internal to the membrane. Further crystal structures of 7TMRs will be slow in coming, certainly much slower than the demands of structural biology and expensive development pathways.

Without a 7TMR's active site geometry, the ligand and substrate discovery process becomes a hit-or-miss proposition. Mutagenesis studies are appropriate for determining the probable active site residues, but without structural information on 7TMRs, the possible ligand set to account for all possible arrangements of those residues can be prohibitively large and does not take into account secondary structural effects on the binding pocket, such as steric hindrance. As a result, ligand choices for possible 7TMRs are painstakingly screened automatically or manually by combinatorial chemistry

systems with thousands of compounds and a low signal-to-noise ratio, despite advances in high-throughput screening and sample preparation.

With the vast advantages that active site geometries or conformations would give both academia and the pharmaceutical industry, why then aren't more researchers devoting time to developing other techniques for structural study of these membrane systems as quickly as possible?

The answer may be that there were many "low-hanging fruit," important soluble proteins or extra-membrane domains that can be studied using the well-developed techniques of solution-state NMR and crystallography. Additionally, high throughput screening (HTS) libraries, during HTS experiments that screen thousands of compounds against 7TMR targets, are often algorithmically selected for sub-libraries of ligands based on several initial first-run ligand binding data. The best-hit "active domains" of these ligands are then further algorithmically combined to form new compounds that are then screened. [35]. Often, this is a more developed, yet expensive, method of establishing a "best fit" ligand for a 7TMR at first pass, before the best hits are handed off to scientific teams for structural and affinity refinement based on more careful binding assays. Undoubtedly, however, structural information on the active site would significantly reduce the cost of such a screening process by offering a more limited ligand choice for HTS screening from the start.

In solid-state NMR, the transfer of information from site to site in a coherent (phase-coupled) manner yields information on internuclear distance, chemical environment, bond angles, and through-bond coupling [36-40]. Despite advances in understanding coherent and non-coherent transfer in solution-phase NMR [41], the thorough characterization of coherence transfer in solids has not yet been extensively studied in the literature. This is most likely due to the experimental difficulties posed by the strong interactions in the solid-state, which until recently obviated the need for any kind of sensitive analysis of exact coupling.

Unfortunately for the studies of 7TMR structures, the methodology of SSNMR is currently not well developed to solve structures without a great deal of sample manipulation. Steady advances in sample preparation, experimental methods and equipment sensitivity are already manifesting the need for more thorough characterization of the coherence transfer process in SSNMR, in order to both develop new experiments as well as refine the current experimental methods. Demands of the “post-genomic age” will require not only high-throughput crystallization procedures for protein structure, but also high-throughput NMR methods; such demands require sample preparation protocols far advanced of the current technology [42] in both solution- and solid-states.

Creative samples to mimic the membrane environment using NMR, aimed at glean structural data on membrane proteins and their ligands, are insinuating themselves in the gray area between solid- and solution-state. Advances in sample handling, materials, and molecular biology have resulted in the development of better methods for preparing artificial membrane environments, such as the "partially aligned" systems in micelles [8], bicelles [43, 44], or lipid bilayers [45]. These "gray area" experiments maintain SSNMR strong coupling in some ways because of these various systems' anisotropic environments [46], making the application of SSNMR theory necessary to separate the information from the "noise" of strong coupling. Such "hybrid" attempts at solving membrane protein structure may ultimately prove successful in the long run [47]; for the moment, however, there needs to be more work on developing the methodology to systematically gain useful information from such systems.

Given the need to develop the methodology to study such challenging biological systems, the focus of this thesis is to examine the strong coupling interactions themselves alone and in various SSNMR established experimental procedures, and to model the interactions in a clear and concise manner which can be later improved on for further experimental development. In the "big picture" of SSNMR, it is absolutely

necessary to define the behavior of a strongly interacting system over time under various experimental situations, including information on where the "hard limits" to useful experimentation exist in the theory.

Specifically, this work focuses both on the behavior of a homonuclear spin- $\frac{1}{2}$ two spin system in SSNMR experiments, which provide distance information between two sites. The systems are analyzed in detail by computing the time development of the density matrix using the product operator formalism for oriented systems, unoriented systems and various dipolar-recoupling experiments including the dipolar, chemical shift, and scalar coupling interactions. Such a host of calculations are not performed for the pure enjoyment of the mathematics, however; there is an immediate need to establish the behavior of these interactions in the solid-state to enable the analysis of experiments for strongly coupled systems of atoms such as complex biological systems. Other studies have succeeded in quantifying coherence transfer in several specific cases [37-39, 48, 49], but before this particular work, no complete study of CT for a two-spin system had been presented in the literature.

This work is scheduled from "easiest" to "hardest," from most specific to most general. Chapter 2 concerns itself with the introduction to the theory of rotational symmetry, the mathematical qualities and characteristics of the general internal Hamiltonians in the solid state, the frame transformations utilized in this thesis, and the characteristic coherent exchange of magnetization. Previous works have done much to address the product operator formalism for various circumstances [41, 50-55] so only a brief introduction to the matrix forms and manipulations of product operators is presented. Chapter 2 acts as the gateway to the subsequent chapters by paving the way for the analytical and numerical simulations provided in this study.

Chapter 3 addresses the simple case of coherent magnetization transfer for the dipolar and scalar coupling interactions in oriented samples. The experimental example of such a system would be a single crystal experiment. Such experiments are not

common, but this examination is necessary to establish the coherent transfer of magnetization in the simplest case and as such an experiment is possible to create in the laboratory, it is not entirely without merit in its own right. Chapter 3 was published in the *Journal of Magnetic Resonance* in 1999 [40], and the cover of that issue, which bears an illustration from the study, can be found in Appendix A.

The single-crystal study prepares the way for Chapter 4, which addresses dipolar and scalar coupling in a two-spin homonuclear unoriented system or a powder sample, alone and with four prior established dipolar-recoupling experiments: DRAMA [56], DRAWS [57], USEME [58] and RFDR [59]. The general case involves a polycrystalline sample as a two-spin homonuclear system with a distribution of preferred directions with strong coupling but no chemical shift. Examples would be the study of selectively labeled and experimentally manipulated membrane proteins in an artificial membrane environment, (for example, multilamellar vesicles) for dipolar recoupling in magic-angle sample spinning (MAS) experiments that refocus the chemical shift interactions.

Chapter 5 addresses the most general set of internal Hamiltonians. It begins with the analysis of a coupled oriented system, and moves to the more general case of a coupled unoriented system in the presence of scalar, dipolar, and chemical shift interactions. This latter case models static two-spin systems, as if we just prepared a sample by perturbing its magnetization away from equilibrium, and watched its response under free evolution decay without any additional experimental manipulation. This is the most extreme example of a strong-coupling Hamiltonian, in which the large entropy “channel” arising from the strong coupling drives the prepared coherent system rapidly into thermal equilibrium. Such a study will be useful in measuring the orientation of a peptide tensor in order to determine the backbone conformation of polypeptides embedded in phospholipid bilayers. For example, the coupling $^{13}\text{C}_{\alpha} - ^{13}\text{C}_{\text{O}}$ parameter can be measured on uniaxially oriented biological solids.

Last, but not least, is Chapter 6, in which results are compared and future directions are proposed. The last chapter attempts to act as a gateway to future studies on multiply-labeled proteins and other SSNMR experimental developments.

CHAPTER 2 CHARACTERISTICS OF COHERENCE TRANSFER THROUGH INTERNAL HAMILTONIANS

Consider two chemically inequivalent homonuclear spin- $1/2$ nuclei in a uniaxially oriented or a single-crystal sample. We assume that the dipolar coupling as well as the scalar coupling between the two nuclei is nonzero. Further, relaxation effects are not considered in the theory. The total Hamiltonian for this system in the presence of a static external magnetic field consists of the isotropic (H_{CS}^{iso}) and anisotropic (H_{CS}^{aniso}) *chemical shift*, which results from the magnetic shielding effect of the electronic bond around the nuclei, *scalar coupling* (H_J), which results from the coupling through the "bucket brigade" of the bonding electrons, *and dipolar coupling* (H_D) which results from the fact that the two nuclei exchange magnetization as if they were two dipoles interacting in one another's fields. The interactions H_D and H_{CS} are anisotropic and therefore have definite directions in space, which is useful in determining information on each nuclei's chemical and physical environment. In this most general case, with all internal Hamiltonians present, we can write the total Hamiltonian as:

$$H_T = H_D + H_J + H_{cs}^{iso} + H_{cs}^{aniso}. \quad (2-1)$$

A full consideration of these Hamiltonians as well as the interactions they represent can be found in several excellent references: Mehring [60], Ernst [41], Gerstein & Dybowski [61], Slichter [62], or Stejskal & Memory [63]. There are also several excellent journal reviews such by Cerf [64] and the Smith, Palke & Grieg series on the Hamiltonians of NMR [65-68].

The success of SSNMR currently depends on reducing or removing the pervasive anisotropy in the total Hamiltonian in Eq. 2-1. Magic-angle sample spinning (MAS) is one such method, which rapidly rotates a sample along an axis that is set to be 54.7° away from the magnetic field axis (reviewed in several sources, c.f. [69]). The spinning frequency must be at least as large as the anisotropic interactions themselves. The end result of successful MAS is that the chemical shift interaction is isotropic in the simplest case, and the dipolar interaction, which is anisotropic by definition, vanishes. During an "ordinary" successful MAS experiment that does not employ special refocusing pulse sequences, the Hamiltonian will only consist of the isotropic parts of the Hamiltonian: the isotropic chemical shift and the scalar coupling, which we will call H_{MAS} [60]

$$H_{\text{MAS}} = H_J + H_{\text{cs}}^{\text{iso}} \quad (2-2)$$

A scaled-down H_D can be recovered during MAS by re-introducing controlled anisotropic interactions into the experiment with specifically designed pulse sequences. These experiments are called magic-angle-spinning dipolar recovery (MASDR) experiments (for instance, [63]). During MASDR experiments, multiple RF pulse sequences are used to selectively recover the dipolar interaction. One such experiment we will consider in Chapter 4 will show that one complete cycle of USEME [58] suppresses the chemical shift interaction, scales the dipolar coupling interaction by a factor of 0.5, and leaves the scalar couplings unaltered.

In the case that the experimental situation, usually utilizing additional pulse sequences with MAS, is created to selectively suppress (refocus) the chemical shift interaction with minimal or no effect on the coupling terms of the total Hamiltonian H_T , the internal Hamiltonian will retain only the terms in the coupling Hamiltonian (H_{JD}) (assuming directly or indirectly bonded spin pairs):

$$H_{\text{JD}} = H_D + H_J \quad (2-3)$$

This Hamiltonian is equivalent to the creation of a zero-field or rotating-frame Hamiltonian in a solid-state NMR experiment. A simple spin echo sequence, in the form

of a series of 180° pulses, can be used to refocus the chemical shifts [60] and leave the scalar as well as the dipolar couplings unaltered. In static solids, usually the scalar coupling term, H_J , is smaller in magnitude than the dipolar coupling term and is often neglected. The scalar coupling becomes important in oriented solid-phase samples especially when the homonuclear dipolar coupling is small, for instance in scaled MASDR experiments. In Chapter 3 we address the coherence transfer resulting from the coupling Hamiltonian. We begin by introducing the convention of the spin operators used in this work.

Introduction to Spin Operators

NMR studies a collection of spins – a population of spins, in fact, which can be considered together as an “ensemble.” This ensemble can be pure (in the case of a system in which all the spins are in the same state) or mixed (in the case of a system where several states are needed to describe different proportions of the total population). In NMR, the density matrix $\sigma(t)$ serves to mathematically describe an ensemble system, which can be either mixed or pure. For an in-depth treatment on density matrices, see a good quantum mechanics book, for example Sakurai [70].

We begin by introducing the mathematical representation of an ensemble. To bring the macroscopic notion of an ensemble as a population of spins to the quantum level, we represent each “pure state” by its own eigenstate. A pure ensemble is a collection of physical systems such that every member of the system can be represented by the same eigenstate $|\alpha\rangle$...in a pure state, the individual spins are non-distinguishable from one another. A mixed ensemble consists of a combination of systems each with a fractional population quantified as “A” which fractional populations are described by their own eigenstates, for example, $\sigma(t) = A_1|\alpha^{(1)}\rangle + A_2|\alpha^{(2)}\rangle + A_3|\alpha^{(3)}\rangle + \dots + A_N|\alpha^{(N)}\rangle$ where N is the number of pure states available to the system and $\sum_N A_n = 1$ is the normalization condition on the fractional populations A_N . A mixed state is therefore a mix of the system eigenstates, each weighted by their fraction of the total population.

How do we express this quantum ensemble of spins? More importantly, how do we relate measurements of mixed quantum ensembles to observables? Using the concept of ensemble averages, which we will not expand here, one can derive the density operator. A density operator ρ is defined by

$$\rho \equiv \sum_N A_N |a^{(N)}\rangle\langle a^{(N)}| \quad (2-4)$$

where “N” is the index of eigenstates of the system. It can be seen that the density operator is constructed from the outer product of the identical individual eigenstates.

The elements of the density matrix can be constructed from the density operator and an arbitrary basis (b) by:

$$\langle b'| \rho | b' \rangle = \sum_N A_N \langle b'| a^{(N)} \rangle \langle a^{(N)} | b' \rangle \quad (2-5)$$

The density matrix for a two-spin-1/2 system can be formed from the outer product of the Pauli matrices σ_x , σ_y and σ_z . The convention used here is that “I” indicates the spin operator for spin #1, and “S” represents the operator for spin #2. The operators indicate the pure state they define. For example, I_x defines the state where all of the population of spin #1 can be described as analogous to the Pauli spin operator σ_x , for example, if the entire system was prepared so that the magnetization of the first spin I was oriented along the “x” direction. An example can be found in Figure 2-1(a) where a representative density matrix has along the top and leftmost column the ket/bra pair that describe each element of the density matrix. Within the elements of the matrix are the operators (sometimes more than one, separated by commas) which have values inside that element of the 4x4, two-spin density matrix. Below, in Fig. 2-1(b) the meanings of each of those elements in terms of what kind of interaction they represent is given. For example, the $|\alpha\beta\rangle\langle\beta\alpha|$ element of the density matrix is a zero-quantum (flip-flop) term whose density operators are $I_x S_y$ and $I_y S_x$. Other combinations, such as the antiphase operators $I_z S_x$ or $I_y S_z$ are not involved in transitions so are not used in this example.

$$\begin{array}{c}
|aa\rangle \quad |a\beta\rangle \quad |\beta a\rangle \quad |\beta\beta\rangle \\
\left[\begin{array}{cccc}
I_z, S_z & S_x, S_y & I_x, I_y & I_{x,y} S_{x,y} \\
S_x, S_y & I_z, S_z & I_{x,y} S_{x,y} & I_x, I_y \\
I_x, I_y & I_{x,y} S_{x,y} & I_z, S_z & S_x, S_y \\
I_{x,y} S_{x,y} & I_x, I_y & S_x, S_y & I_z, S_y
\end{array} \right]
\end{array} \quad (a)$$

$$\begin{array}{c}
|aa\rangle \quad |a\beta\rangle \quad |\beta a\rangle \quad |\beta\beta\rangle \\
\left[\begin{array}{cccc}
\text{Pop} & \text{SQS} & \text{SQI} & \text{DQ} \\
\text{SQS} & \text{Pop} & \text{ZQ} & \text{SQI} \\
\text{SQI} & \text{ZQ} & \text{Pop} & \text{SQS} \\
\text{DQ} & \text{SQI} & \text{SQS} & \text{Pop}
\end{array} \right]
\end{array} \quad (b)$$

Figure 2-1: Operators important to NMR transitions. Compare with the individual operators shown in Table 2-1. (a) Density matrix from the Pauli spin matrices with the notation for I and S operators included. The usual convention, that of α "spin down" and β "spin up" applies. (b) the meanings of each of the operators in terms of population (Pop), single quantum I or S (SQ I, SQ S), zero quantum (ZQ) and double quantum (DQ) populations. Space-saving notation $X_{n,m}Y_{n,m}$ means to include all combinations of operators in that element, as an example $I_{x,y}S_{x,y}$ stands for operators I_xS_y , I_yS_x , I_xS_x , I_yS_y .

A complete list of operators in matrix format are shown in Table 2-1.

How does the density operator change with time? Given an initial state $\sigma(0)=I_x$, for example, how will this state evolve under free precession? One begins with Liouville's theorem for density matrices in classical statistical mechanics,

$$\frac{\partial \mathbf{s}_{classical}}{\partial t} = -[\mathbf{s}_{classical}, H]_{classical} \quad (2-6)$$

with $\sigma_{classical}$ as density of the representative points in phase space and H as the interacting Hamiltonian, has an exact quantum mechanical analogue in the Liouville-von Neuman equation:

$$\frac{\partial \mathbf{s}}{\partial t} = -\frac{i}{\hbar}[\mathbf{s}, H] \quad (2-7)$$

meaning that the change in the state of the density operator with time depends on the commutator with the system's Hamiltonian. In the case of free evolution, the Hamiltonian would be the internal interactions, or "internal Hamiltonian."

Table 2-1: The two-spin operators as density matrices.

$$\begin{array}{ll}
 E = \frac{1}{4} \begin{bmatrix} 1 & 0 & 0 & 0 \\ 0 & 1 & 0 & 0 \\ 0 & 0 & 1 & 0 \\ 0 & 0 & 0 & 1 \end{bmatrix} & S_x = \frac{1}{4} \begin{bmatrix} 0 & 1 & 0 & 0 \\ 1 & 0 & 0 & 0 \\ 0 & 0 & 0 & 1 \\ 0 & 0 & 1 & 0 \end{bmatrix} \\
 S_y = \frac{i}{4} \begin{bmatrix} 0 & -1 & 0 & 0 \\ 1 & 0 & 0 & 0 \\ 0 & 0 & 0 & -1 \\ 0 & 0 & 1 & 0 \end{bmatrix} & S_z = \frac{1}{4} \begin{bmatrix} 1 & 0 & 0 & 0 \\ 0 & -1 & 0 & 0 \\ 0 & 0 & 1 & 0 \\ 0 & 0 & 0 & -1 \end{bmatrix} \\
 I_x = \frac{1}{4} \begin{bmatrix} 0 & 0 & 1 & 0 \\ 0 & 0 & 0 & 1 \\ 1 & 0 & 0 & 0 \\ 0 & 1 & 0 & 0 \end{bmatrix} & I_x S_x = \frac{1}{4} \begin{bmatrix} 0 & 0 & 0 & 1 \\ 0 & 0 & 1 & 0 \\ 0 & 1 & 0 & 0 \\ 1 & 0 & 0 & 0 \end{bmatrix} \\
 I_x S_y = \frac{i}{4} \begin{bmatrix} 0 & 0 & 0 & -1 \\ 0 & 0 & 1 & 0 \\ 0 & -1 & 0 & 0 \\ 1 & 0 & 0 & 0 \end{bmatrix} & I_x S_z = \frac{1}{4} \begin{bmatrix} 0 & 0 & 1 & 0 \\ 0 & 0 & 0 & -1 \\ 1 & 0 & 0 & 0 \\ 0 & -1 & 0 & 0 \end{bmatrix} \\
 I_y = \frac{i}{4} \begin{bmatrix} 0 & 0 & -1 & 0 \\ 0 & 0 & 0 & -1 \\ 1 & 0 & 0 & 0 \\ 0 & 1 & 0 & 0 \end{bmatrix} & I_y S_x = \frac{i}{4} \begin{bmatrix} 0 & 0 & 0 & 1 \\ 0 & 0 & -1 & 0 \\ 0 & 1 & 0 & 0 \\ 1 & 0 & 0 & 0 \end{bmatrix} \\
 I_y S_y = \frac{1}{4} \begin{bmatrix} 0 & 0 & 0 & -1 \\ 0 & 0 & 1 & 0 \\ 0 & 1 & 0 & 0 \\ -1 & 0 & 0 & 0 \end{bmatrix} & I_y S_z = \frac{i}{4} \begin{bmatrix} 0 & 0 & -1 & 0 \\ 0 & 0 & 0 & 1 \\ 1 & 0 & 0 & 0 \\ 0 & -1 & 0 & 0 \end{bmatrix} \\
 I_z = \frac{1}{4} \begin{bmatrix} 1 & 0 & 0 & 0 \\ 0 & 1 & 0 & 0 \\ 0 & 0 & -1 & 0 \\ 0 & 0 & 0 & -1 \end{bmatrix} & I_z S_x = \frac{1}{4} \begin{bmatrix} 0 & 1 & 0 & 0 \\ 1 & 0 & 0 & 0 \\ 0 & 0 & 0 & -1 \\ 0 & 0 & -1 & 0 \end{bmatrix} \\
 I_z S_y = \frac{i}{4} \begin{bmatrix} 0 & -1 & 0 & 0 \\ 1 & 0 & 0 & 0 \\ 0 & 0 & 0 & 1 \\ 0 & 0 & -1 & 0 \end{bmatrix} & I_z S_z = \frac{1}{4} \begin{bmatrix} 1 & 0 & 0 & 0 \\ 0 & -1 & 0 & 0 \\ 0 & 0 & -1 & 0 \\ 0 & 0 & 0 & 1 \end{bmatrix}
 \end{array}$$

A formal solution of the Liouville-von Neuman equation, with the restrictions of a time-independent, internally commuting Hamiltonian, involves exponentials.

$$\mathbf{S}(t) = \exp\left(-\frac{i}{\hbar} Ht\right) \mathbf{S}(0) \exp\left(\frac{i}{\hbar} Ht\right) \quad (2-8)$$

In NMR experiments, the Hamiltonian can be expressed in terms of the same density operators shown in Table 2-1. Therefore, the time evolution of the density matrix involves exponentials of matrix operators. For example, if we assume we are observing a system in its interaction frame, and the system has been prepared in the I_x pure state by selective pulse sequences, then the density operator at time zero is $\sigma(0)=I_x$. If our Hamiltonian is the Zeeman interaction, where $H = -\hbar\omega_0 I_z$, then the complete expression for the density matrix is:

$$\mathbf{S}(t) = \exp(-i\omega_0 t I_z) I_x \exp(i\omega_0 t I_z) \quad (2-9)$$

The exponentials act as operators on the pure state I_x . Operations with exponentials in this case are akin to rotations in the operator space, where in this case I_x is rotated around the "Iz axis" by an angle $\omega_0 t$. A full exposition on rotational matrices and angular momentum operators can be found in sources such as Brink and Satchler [71] or Rose [72]. The formal operation of this equation involves expanding out the exponentials to a reasonable number of terms, multiplying the matrices, and then doing significant simplification to arrive at the final answer. Luckily, a simpler algorithm has been developed which makes shorthand out of these kinds of calculations. For a full development of exponential operators and the mathematical formalism behind their operation, see for instance Gerstein & Dybowski [61]. The shorthand formalism for calculating the new state after interaction with a Hamiltonian is

$$O_p \xrightarrow{(\theta)O_q} \begin{cases} O_p & \text{If } [O_p, O_q]=0 \\ O_p \cos(\theta) + i[O_p, O_q] \sin(\theta) & \text{If } [O_p, O_q] \neq 0 \end{cases} \quad (2-10)$$

where the operator O_p is the original operator (for instance, I_x) and the O_q are the operator(s) within the Hamiltonian. When O_p commutes with O_q , the resulting operator is just the original state. When the two operators do not commute, a mixed state is generated, where the original operator is modulated by the cosine with a frequency equal to the coefficient of the Hamiltonian operator, plus another sine-modulated term which results from the commutation of the Hamiltonian operator and the original operator (recall the Liouville-von Neumann equation). This is a subtle but important point in understanding the changes to a pure state under the action of a non-commuting operator. This "master equation" can be applied sequentially when there are more than one operators within the Hamiltonian, as long as the operators within the Hamiltonian commute with one another. Fortunately, in the case of most of this work, we will examine Hamiltonians with internally commuting operator sets. In Chapter 5, however, the case of a non-internally commuting Hamiltonian is considered, in which we must first diagonalize the Hamiltonian in a new basis by switching to a rotated "interaction frame." We will go into more detail in Chapter 5.

Characteristics of the Spin Component of the Dipolar Hamiltonian

We begin our investigation of coherence transfer by examining some important characteristics of the dipolar Hamiltonian. Consider the rotation operator space of two spin $\frac{1}{2}$ nuclei, which is defined by 16 Cartesian product operators that form a closed $SU(2) \times SU(2)$ group under matrix multiplication and commutation. In Chapter 3, we present the DCT of an oriented system that results from the operations of the dipolar Hamiltonian on an initial state, $\sigma(0)$ where $\sigma(0)$ is the thermal equilibrium or initial density matrix at time zero. We term the operators that evolve from $\sigma(0)$ with the interacting Hamiltonian the "resultants" as shorthand.

The dipolar coupling Hamiltonian can be expressed in the form of spherical tensors:

$$H_D = \sum_{q=-2}^{+2} (-1)^q D_{2q} T_{2-q} \quad (2-11)$$

where the second-rank tensors D_{2q} and T_{2q}^2 define the spatial and spin parts of the dipolar coupling Hamiltonian [60]. The secular dipolar coupling Hamiltonian in the dipolar coupling tensor principal axis system can be given as:

$$H_D = \frac{\hbar \gamma_I \gamma_S}{4 \pi r_{IS}^3} [1 - 3 \cos^2 \theta] (3I_z S_z - I \cdot S) \quad (2-12)$$

where θ is the angle between the magnetic field and the internuclear vector, r_{IS} is the distance between I and S nuclei, and γ_i is the gyromagnetic ratio of nucleus i. Since the mathematical structure of the direct (H_D) and indirect (H_J) coupling Hamiltonians for a homonuclear spin system is similar, the total coupling Hamiltonian is given as

$$H_{JD} = (2D_{IS} + J)I_z S_z - (D_{IS} - J)\{I_x S_x + I_y S_y\} \quad (2-13)$$

where J is the scalar coupling constant and D_{IS} is the dipolar coupling frequency defined as

$$D_{IS} = \frac{\hbar \gamma_I \gamma_S}{4 \pi r_{IS}^3} [1 - 3 \cos^2 \theta] \quad (2-14)$$

In order to evaluate the coherence transfer modes due to the evolution under the coupling Hamiltonian, we assume a uniaxially oriented system with $\theta = 0^\circ$. Any change in the value of θ will only change the magnitude of the D_{IS} parameter.

Rotation and Commutation of Operators and the Dipolar Hamiltonian

Initial states that commute with all but one operator ($I_x S_x$, $I_y S_y$, or $I_z S_z$) in the Hamiltonian of Equation 2-13 will undergo DCT analogous to the scalar coupling case

in which the Hamiltonian is isotropic. This isotropic behavior results in a conservation of coherence, restricting the coherence transfer to a three-member subgroup: the spin operator of the initial state $\sigma(0)$, the single operator from the isotropic Hamiltonian, and the resultant operator. These three operators form a true cyclic symmetry group. We define a “weak-coupling subgroup” as defined by the initial state $\sigma(0)$, a single non-commuting Hamiltonian operator, and the resulting commutator (we assume inclusion of negatives). This is similar to the case of weak scalar coupling in solution-state NMR Hamiltonians, when the scalar coupling Hamiltonian is equal to $IzSz$.

Weak-coupling DCT forms a non-trivial four-member subgroup under rotation (and therefore commutation), including the identity operator, resulting in DCT that is kept internal to the subgroup with the resultants modulated by a single frequency, for example:

$$I_z \xrightarrow{\omega t(2I_zS_z - 2I_yS_y)} I_z \cos(\omega t) + 2iI_xS_y \sin(\omega t) \quad (2-15)$$

where ω is a frequency, for instance, defined by the spatial component of the dipolar Hamiltonian. Since $IzSz$ commutes with Iz , the resulting subgroup for Eq. 2 is E , Iz , $IySy$ and $IxSy$.

Strong-coupling subgroups originate from $\sigma(0)$ that do not commute with at least two of the operators in the Hamiltonian. In a strong-coupling DCT subgroup, it can be seen from Tables 2-3 through 2-5 that the resultant operators plus the generators ($IzSz$, $IySy$, and $IxSx$ from the dipolar Hamiltonian) form closed subgroups, labeled by the initial state $\sigma(0)$. The “commutator” operator is defined as the Hamiltonian operator that commutes with all members of the subgroup and therefore defines the subgroup space, which is closed under rotation. It happens that strong coupling *operations conserve coherence* within this 7-member rotational subgroup. We will see in Chapter 5 that coherence is lost when this symmetry is broken.

Because all operators in the sixteen-spin space commute with only one operator in the Hamiltonian, all initial states $\sigma(0)$ under the dipolar Hamiltonian evolve into resultant operators within one of the I_xS_x , I_yS_y , or I_zS_z rotational subgroups. Tables 2-3 through 2-5 give the entire dot product symmetries for each of the groups operating under the dipolar Hamiltonian. These symmetries show the limiting nature of the different groups operating with the dipolar Hamiltonian; one can never generate an I_y coherence, for example, while within the I_z subgroup (Table 2-5). The tables can be read sequentially; that is, take the leftmost column to be the operator acting on the topmost row; for example, in Table 2-3, the dot product of I_x (leftmost column) and I_zS_z (upper row) is I_yS_z . This is identical to saying that the sequential rotation of a fictitious magnetization vector along I_x then along I_zS_z yields I_yS_z . These tables show that each operator within each of the subgroups outlined in Table 2-2 maintains the identity of a rotation group under the dot product. The conservation of rotation is apparent from the tables.

Table 2-2: The definition of the subgroups generated by a Hamiltonian in a two-spin-1/2 space. We have not included the negative forms of the operators for brevity but it should be assumed that all members of the subgroups include all negative forms of the operators.

COMMUTATOR	GENERATOR	SUBGROUP MEMBERS
I_xS_x	I_zS_z, I_yS_y	$E, I_x, S_x, I_yS_z, I_zS_y, I_zS_z, I_yS_y$
I_yS_y	I_zS_z, I_xS_x	$E, I_y, S_y, I_xS_z, I_zS_x, I_zS_z, I_xS_x$
I_zS_z	I_xS_x, I_yS_y	$E, I_z, S_z, I_xS_y, I_yS_x, I_xS_x, I_yS_y$

All product operators should be multiplied by 2.

For example, a particular MASDR dipolar Hamiltonian has a spin part where $H_{\text{spin}} = I_yS_y + I_zS_z$, so the only operators that will experience strong-coupling DCT in this case are those in the I_xS_x commutator group in Table 2-2. For instance, when $\sigma(0) = I_x$, the evolution produces resultants of I_x, S_x, I_zS_y and I_yS_z , shown in Eq. 2-16.

Tables 2-3 through 2-5. Inner products of the I_x , I_y , and I_z group of matrices. (Note that these are not commutators). The inner product for each combination can be found within the table row/column corresponding to the pair: start with the bold operator in the leftmost column and dot it with the operator in the topmost row to yield the dot product in the table. The sub-group common to all is shaded. For example, in Table 2-3, $I_x \cdot I_z S_z = I_y S_z$. See text.

Table 2-3: Inner product (dot product) group characteristic table for I_x group matrices.

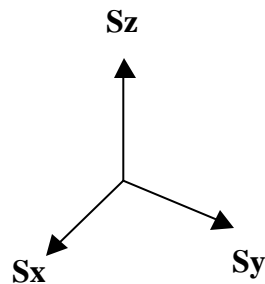
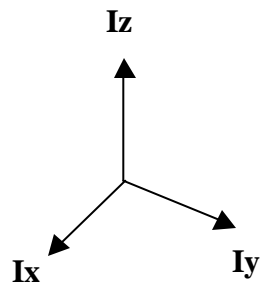
	$I_z S_z$	$I_x S_x$	$I_y S_y$	I_x	S_x	$I_y S_z$	$I_z S_y$
$I_z S_z$	E	$I_y S_y$	$I_x S_x$	$-I_y S_z$	$-I_z S_y$	I_x	S_x
$I_x S_x$	$I_y S_y$	E	$I_z S_z$	S_x	I_x	$-I_z S_y$	$-I_y S_z$
$I_y S_y$	$I_x S_x$	$I_z S_z$	E	$I_z S_y$	$I_y S_z$	$-S_x$	$-I_x$
I_x	$I_y S_z$	S_x	$-I_z S_y$	E	$I_x S_x$	$-I_z S_z$	$I_y S_y$
S_x	$I_z S_y$	I_x	$-I_y S_z$	$I_x S_x$	E	$I_y S_y$	$-I_z S_z$
$I_y S_z$	$-I_x$	$-I_z S_y$	S_x	$I_z S_z$	$-I_y S_y$	E	$-I_x S_x$
$I_z S_y$	$-S_x$	$-I_y S_z$	I_x	$-I_y S_y$	$I_z S_z$	$-I_x S_x$	E

Table 2-4: Inner product (dot product) group characteristic table for I_y group matrices.

	$I_z S_z$	$I_x S_x$	$I_y S_y$	I_y	S_y	$I_x S_z$	$I_z S_x$
$I_z S_z$	E	$I_y S_y$	$I_x S_x$	$I_x S_z$	$I_z S_x$	$-I_y$	$-S_y$
$I_x S_x$	$I_y S_y$	E	$I_z S_z$	$-I_z S_x$	$-I_x S_z$	S_y	I_y
$I_y S_y$	$I_x S_x$	$I_z S_z$	E	S_y	I_y	$-I_z S_x$	$-I_x S_z$
I_y	$-I_x S_z$	$I_z S_x$	S_y	E	$I_y S_y$	$I_z S_z$	$-I_x S_x$
S_y	$-I_z S_x$	$I_x S_z$	I_y	$I_y S_y$	E	$-I_x S_x$	$I_z S_z$
$I_x S_z$	I_y	$-S_y$	$-I_z S_x$	$-I_z S_z$	$I_x S_x$	E	$-I_y S_y$
$I_z S_x$	S_y	$-I_y$	$-I_x S_z$	$I_x S_x$	$-I_z S_z$	$-I_y S_y$	E

Table 2-5: Inner Product (dot product) group characteristic table for I_z group matrices.

	$I_z S_z$	$I_x S_x$	$I_y S_y$	I_z	S_z	$I_x S_y$	$I_y S_x$
$I_z S_z$	E	$I_y S_y$	$I_x S_x$	S_z	I_z	$-I_y S_x$	$-I_x S_y$
$I_x S_x$	$I_y S_y$	E	$I_z S_z$	$I_y S_x$	$I_x S_y$	$-S_z$	$-I_z$
$I_y S_y$	$I_x S_x$	$I_z S_z$	E	$-I_x S_y$	$-I_y S_x$	I_z	S_z
I_z	S_z	$-I_y S_x$	$I_x S_y$	E	$I_z S_z$	$-I_y S_y$	$I_x S_x$
S_z	I_z	$-I_x S_x$	$I_y S_x$	$I_z S_z$	E	$I_x S_x$	$-I_y S_y$
$I_x S_y$	$-I_y S_x$	S_z	$-I_z$	$I_y S_y$	$-I_x S_x$	E	$-I_z S_z$
$I_y S_x$	$-I_x S_y$	I_z	$-S_z$	$-I_x S_x$	$I_y S_y$	$-I_z S_z$	E



$$I_x \xrightarrow{wt(2I_zS_z-2I_yS_y)} \frac{1}{2}[I_x \cos(2\omega t) + (I_yS_z - I_zS_y)(\sin(2\omega t)) + S_x(1 - \cos(2\omega t))] \quad (2-16)$$

It can be seen, therefore, that the dipolar interaction, with its cylindrically symmetric Hamiltonian, is able to generate a group of operators which transfer coherence within a small subgroup of the 16-operator space, thereby conserving coherence among a subset of the operators. This conservation of coherence in the form of magnetization energy due to the symmetry of the secular dipolar Hamiltonian brings to mind Noether's Theorem, which states that energy conservation results from symmetry [70]. Therefore, we should expect that perturbations to the symmetry of the Hamiltonian (such as introduction of nonsecular terms or additional non-symmetric Hamiltonian terms) will result in coherence shared among more members of the density matrix, reducing the overall signal in any one coherence and reducing the usefulness of coherence transfer. We will examine a specific case of this, when we superpose chemical shifts with the dipolar Hamiltonian in Chapter 5.

Characteristics of the Spatial Component of the Dipolar Hamiltonian

The spin operators of MASDR experiments are time-modulated by frequencies that are calculated from the spatial component of the dipolar Hamiltonian.

$$\mathbf{w}(\mathbf{q}, \mathbf{j}) = \frac{g_N^2 \hbar}{r^3} F(\mathbf{q}, \mathbf{j}) \quad (2-17)$$

The angular dependency of the spatial component takes on the general form of a linear combination of spherical harmonics

$$F_D(\mathbf{q}, \mathbf{j}) = \sum_{l,m} a_{lm} Y_{lm} \quad (2-18)$$

where $l = 0, 1, 2$ and $m = \{-2, -1, 0, 1, 2\}$ with normalized coefficients a_{lm} that range in value from 0 to 1. The Euler angles $(\alpha_D, \beta_D, \gamma_D)$ orient the principal axis system of the dipolar coupling tensor to the goniometer axis system and are represented with $(0, \theta, \varphi)$ (the dipolar tensor's uniaxial symmetry requires that $\alpha_D = 0$).

To calculate the effects of MASDR pulse sequences on the dipolar Hamiltonian, the principal-axis expression of the dipolar Hamiltonian

$$H_D = \frac{\hbar \gamma_I \gamma_S}{4 \pi r_{IS}^3} [1 - 3 \cos^2 \theta] (3 I_z S_z - I \cdot S) \quad (2-19)$$

should be rotated into the interaction representation using Wigner rotation matrices \mathfrak{R} [41, 60, 62] for the transformation:

$$\mathbf{w}_0^{I,L} = \sum_m \mathbf{w}_m^{I,D} \mathfrak{R}_{m0}^2(\Omega_{DL}) \quad (2-20)$$

where θ_m is the angle between the goniometer axis and the magnetic field. With the Wigner matrices, the spatial component of the dipolar Hamiltonian are rotated into the form

$$\begin{aligned} D^{LAB} = d_{IS} & \left(\frac{3}{4} \sin^2 \mathbf{q}_m \sin^2 \mathbf{q} \cos(2\mathbf{w}_r t + 2\mathbf{j}) \right. \\ & - \frac{3}{4} \sin 2\mathbf{q}_m \sin 2\mathbf{q} \cos(\mathbf{w}_r t + \mathbf{j}) \\ & \left. + \frac{1}{4} (3 \cos^2 \mathbf{q}_m - 1)(3 \cos^2 \mathbf{q} - 1) \right) \end{aligned} \quad (2-21)$$

where θ_m is the angle between the goniometer axis and the magnetic field . The derivation of Eq. 2-21 will be explored in more detail in Chapters 4 and 5.